# Sensor Concept Based on Piezoelectric PVDF Films for the Structural Health Monitoring of Fatigue Crack Growth

**Dennis Bäcker**[1]**, Andreas Ricoeur**[2] **and Meinhard Kuna**[1]

**Abstract:**   A new sensor concept for monitoring fatigue crack growth in technical structures is presented. It allows the in-situ determination of the position of the crack tip as well as the fracture mechanical quantities. The required data are obtained from a piezoelectric polymer film, which is attached to the surface of the monitored structure. The stress intensity factors and the crack tip position are calculated from electrical potentials obtained from a sensor array by solving the non-linear inverse problem.

**Keywords:**   fatigue crack growth, fracture mechanical sensor, stress intensity factors, SIF sensor, PVDF, structural health monitoring.

## 1   Introduction

The life cycle of technical structures under deterministic or stochastic loads is often limited by crack growth. Considering the failure of technical structures subcritical fatigue crack growth often plays an essential role [Lange  (1983)]. To ensure the guaranteed minimum life cycle of machines and plants the growth rates of expected or observed fatigue cracks must be known. Due to the mostly occurring stochastic load collectives and complex geometries predictions based on pure calculation are problematic. In particular, civil engineering constructions, aircraft structures, vehicles as well as wind turbines are exposed to complex load collectives. Numerical stress analyses are inexact due to uncertainties in the load assumptions [Kamleitner et al.  (2005)]. Therefore, expensive inspections of highly loaded structural components with respect to cracks are regularly required.

Different methods have been developed for the monitoring of the structural integrity including those to evaluate cracks. On the one hand, there are methods detecting

---

[1] Technische Universität Bergakademie Freiberg, Institute of Mechanics and Fluid Dynamics, Lampadiusstrasse 4, 09599 Freiberg, Germany.

[2] Universität Kassel, Institute of Mechanics, Mönchbergstraße 7, 34125 Kassel, Germany.

just the size and location of cracks, on the other there are those quantifying the stress state at the crack tip. Concepts for the determination of crack length and position are using different physical effects. Some are based on the interaction principle of high-frequency mechanical waves with the crack. Often piezoelectric or magnetostrictive [Kwun et al. (2002)] components are used for the generation of these waves and the detection of the signals modified by the crack. With an appropriate processing of the signals the crack position is determined. The crack length can be e.g. obtained from the signal of a strain gauge ([Gama and Morikawa (2008)], [Kurosaki et al. (2002)]) supplying information on the crack length-dependent stiffness of the specimen. There are also methods for the experimental determination of fracture mechanical quantities e.g. stress intensity factors (SIF). These include photo elastic methods ([Lu and Chiang (1993)], [Singh and Shuka (1996)]), laser interferometry and the caustic method [Shozu et al. (2002)] as well as thermo elastic stress methods. However, those methods are not suitable for efficient long-term monitoring of technical structures. Thermal methods use electromagnetic infrared radiation emitted from the surface of a specimen, which is particularly observed in the fracture process zone. Thus, the stress distributions are determined and SIF are calculated ([Shiratori et al. (1990)], [Honda et al. (2002)]). Some optical methods correlate images of the crack growth using digital image processing technology and thus determine the fracture mechanical quantities ([McNeill et al. (1987)], [Rethore et al. (2005)], [Roux and Hild (2006)]) by appropriate evaluation. A rarely used method for SIF determination is based on the measurement of the potential difference at the crack, which occurs due to the skin effect if a high frequent alternating current is applied [Saka et al. (1991)]. The use of strain gauges, mostly applied in front of the crack tip, is one of the most frequent methods to determine SIFs ([Irwin (1957)], [Dally and Sanford (1988)], [Dally and Sanford (1990)], [Putra (2000)]). However, it is not suitable for a long-term monitoring of structures in service, since crack growth must be excluded. Particularly, a high spatial resolution can not be attained. In addition, a high cabling effort is required, which is mainly due to the obligatory external energy source. Some new concepts exploit piezoelectric polymer films as sensors for the experimental determination of fracture mechanical quantities ([Fujimoto et al. (2003)], [Fujimoto et al. (2003)], [Fujimoto et al. (2004)]). They compensate for disadvantages of classical resistance strain gauges, are easily applied and are optimally suitable for long-term monitoring. However, recently developed concepts based on piezoelectric polymers merely aim at the experimental determination of SIFs for a given crack length and do not include crack growth into consideration.

## 2   Piezoelectric polymer material PVDF

Polyvinylidene fluoride (PVDF) is efficiently applicable as actuator or sensor. The chemical basic molecule -$(CH_2CF_2)_n$- exhibits a strong electronegativity of the fluorine compared to the carbon. Thereby, the $CF_2$- dipoles are aligned perpendicularly to the molecular chain axis (Fig. 1), attaining a maximum of polarization in the $\beta\hat{A}$-modification of PVDF [Danz and Geiss  (1987)]. Macroscopic piezoelectric properties of the polymeric material are obtained by the polarization process, where in most cases a mechanical extension superimposes an electric field in the thickness direction.
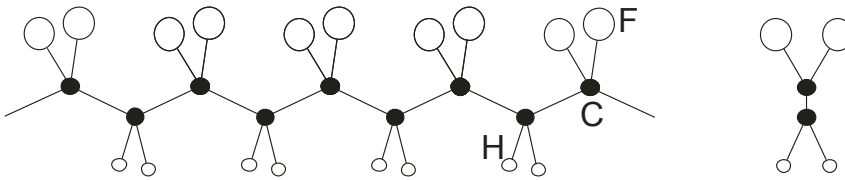


Figure 1: Molecular structure of PVDF in $\beta$ - modification

The piezoelectric and dielectric properties of PVDF are comparable to those of ceramic piezoelectrics, the mechanical properties are much different, though. Due to the anisotropy in the 1-2-plane caused by production the material is orthotropic. The small elastic modulus and the extremely low mass of the sensor material open up new application fields compared to piezoelectric ceramics. Due to simple adhesive attachment and the high flexibility of the layer an application on any curved surface is feasible. The temperature range for an application of PVDF films as actuators or sensors is between -70˚C and +90˚C. However, PVDF exhibits strong pyroelectric properties. The resulting high temperature sensitivity must be taken into account and should be compensated during measurements. Special design of the coating of the polymer layer allows for the construction of complex sensor arrays accomplishing a high spatial resolution.

The material constants of PVDF were taken from [Roh et al.  (2002)]. Within the framework of a thermodynamically consistent material modelling they are transformed with respect to strain and electric field as independent variables (see appendix).

## 3   Material equations for an orthotropic piezoelectric sensor

Based on the independent variables $\varepsilon_{ij}$ (strain) and $E_i$ (electric field) the piezoelectric material behavior can be expressed by the following constitutive equations:

$$\sigma_{ij} = c_{ijkl}\varepsilon_{kl} - e_{kij}E_k$$
$$D_i = e_{ikl}\varepsilon_{kl} + \kappa_{ij}E_j \tag{1}$$

The elasticity tensor $c_{ijkl}$ represents the partial derivative of stresses $\sigma_{ij}$ with respect to strain at constant electric field and the dielectric tensor $\kappa_{ij}$ is the derivative of the electric displacement $D_i$ with respect to the electric field at constant strain. The third order piezoelectric tensor $e_{kij}$ describes the coupling of mechanical and electrical fields. In Voigt notation all tensors are represented by matrices as shown in the appendix. This notation clarifies the orthotropic material behavior concerning both mechanical and electrical properties.

For the film $x_3$ is chosen as polarization direction (Fig. 2), the axes 1 and 2 are lying in-plane. Furthermore, the plane stress state is assumed to prevail in the film ($\sigma_{33} = 0$).

Since the polarization is orientated into the 3-direction and the potentials can be measured only at the surfaces, the $x_3$-component of the electric field is relevant. From the constitutive relations (1) the following equations can be derived:

$$\sigma_{33} = c_{31}\varepsilon_{11} + c_{32}\varepsilon_{22} - e_{33}E_3 = 0 \tag{2}$$

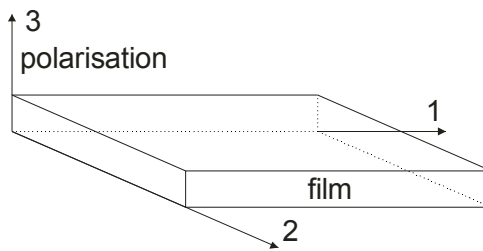$$D_3 = e_{31}\varepsilon_{11} + e_{32}\varepsilon_{22} + e_{33}\varepsilon_{33} + \kappa_{33}E_3 \tag{3}$$



Figure 2: Piezoelectric film with coordinate system

By eliminating $\varepsilon_{33}$ from Eqs. (2) and (3), the dependence of the electric field perpendicular to the sensor film from the in-plane strain is obtained

$$E_3 = C_1\varepsilon_{11} + C_2\varepsilon_{22} + C_3D_3 \tag{4}$$

with the constants $C_1, C_2, C_3$:

$$C_1 = \frac{c_{31}e_{33} - c_{33}e_{31}}{e_{33}^2 + k_{33}c_{33}} \tag{5}$$

$$C_2 = \frac{c_{32}e_{33} - c_{33}e_{32}}{e_{33}^2 + k_{33}c_{33}} \tag{6}$$

$$C_3 = \frac{c_{33}}{e_{33}^2 + k_{33}c_{33}} \tag{7}$$

In the following, it is assumed that no free charges accumulate at the film surface such that $D_3 = 0$.

For sensory applications a potential difference $\Delta\phi_{AB} = \phi_A - \phi_B$ is measured between the lower and upper film surface (Fig. 3).
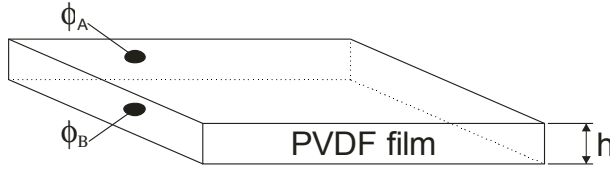


Figure 3: Potential difference across the film thickness

This coincides with the voltage $U_{AB}$ by definition. For linear potential gradient in the thickness direction the electrical field is calculated as follows:

$$E_3 = -\nabla\phi = -\frac{\Delta\phi_{AB}}{h}, \tag{8}$$

with $h$ as film thickness.

With equation (4) the measured voltage at the film is given as:

$$U_{AB} = -h(C_1\varepsilon_{11} + C_2\varepsilon_{22}). \tag{9}$$

## 4   Relations for a transversely isotropic sensor film arrangement

For isotropic material behavior Eq. (9) can be simplified as

$$U_{AB} = -hC(\varepsilon_{11} + \varepsilon_{22}), \tag{10}$$
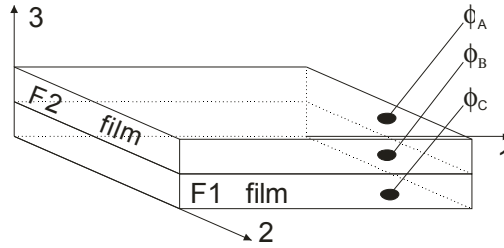
with $C = C_1 = C_2$.

Figure 4: Two stacked orthotropic films. Material axes of the upper film rotated by 90° with respect to the lower film

A transverse isotropy is obtained if two orthotropic films are rotated by 90° to each other before gluing them (Fig. 4).

Starting from Eq. (8) applied to each film gives the relation

$$U_{AC} = -(E_3^{F1}h^{F1} + E_3^{F2}h^{F2}). \tag{11}$$

Assuming that both films have the same thickness i. e. $h^{F1} = h^{F2} = h$ it follows:

$$U_{AC} = -hC^*(\varepsilon_{11} + \varepsilon_{22}), \tag{12}$$

with $C^* = \frac{(c_{31}+c_{32})\,e_{33}-(e_{31}+e_{32})\,c_{33}}{\left(e_{33}^2+k_{33}c_{33}\right)}$

## 5   Relationship between stresses within the specimen and the electric potential difference

Due to the adhesive bonding of the sensor film to the specimen it can be ideally assumed that the strains from the surface of the specimen are transmitted to the film without sliding. Generally this is probably not the case, since the adhesive layer between the specimen and the film represents a joint with viscoplastic properties. The discontinuity of the displacements $u_1$, $u_2$ at the interface can be taken into account by the very simple linear relationship with $g \leq 1$

$$\varepsilon_{ij}^F = g\varepsilon_{ij}^S \quad (i = j) \tag{13}$$

where the superscript $F$ represents the film and $S$ stands for the structure.

In the case that the film coordinate system is rotated with respect to the crack coordinate system, the specimen surface strains have to be transformed into the film coordinate system:

$$\varepsilon_{11}^F = g\left(\varepsilon_{11}^S \cos^2\beta + \varepsilon_{22}^S \sin^2\beta + 2\varepsilon_{12}^S \sin\beta\,\cos\beta\right) \tag{14}$$
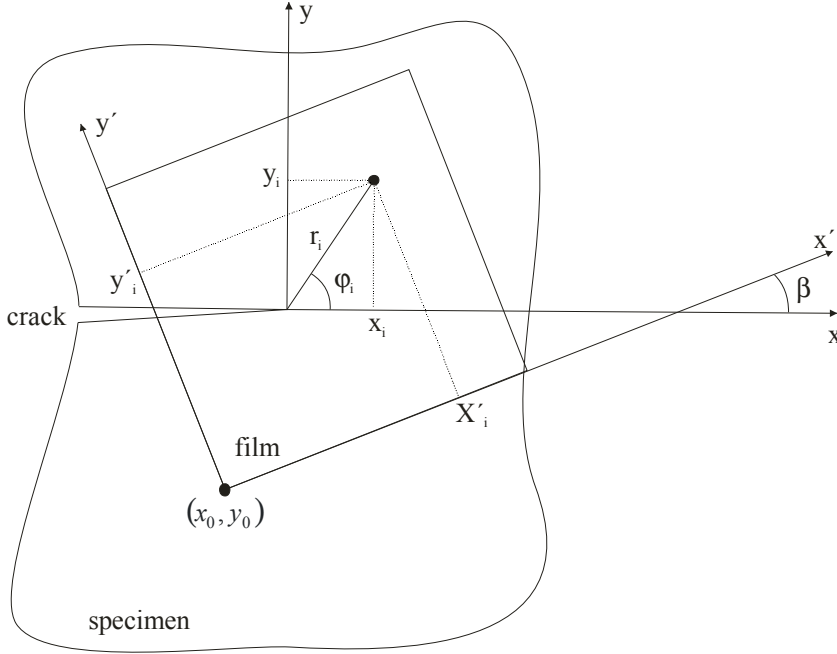
Figure 5: Crack coordinate system $(x, y)$ and film coordinate system $(x', y')$

Here, the angle $\beta$ is the angle of rotation between both coordinate systems (Fig. 5). Assuming a plane stress state at the surface of the specimen it is

$$\varepsilon_{12}^S = \frac{\left(1 + v^S\right)}{E^S} \sigma_{12}. \tag{15}$$

With the elastic modulus $E^S$ and Poison's ratio $v^S$.

Substituting Eqs. (16) to (15) into (14), (15) and finally into (9), the voltage

$$
\begin{aligned}
U_{AB} = -\frac{hg}{E^S} \Big\{ &\sigma_{11} \left[ cos^2\beta \left( C_1 - v^S C_2 \right) + sin^2\beta \left( C_2 - v^S C_1 \right) \right] + \\
&\sigma_{22} \left[ sin^2\beta \left( C_1 - v^S C_2 \right) + cos^2\beta \left( C_2 - v^S C_1 \right) \right] + \\
&\sigma_{12} \left( 1 + v^S \right) \left( C_1 - C_2 \right) sin\left( 2\beta \right) \Big\}
\end{aligned}
\tag{16}
$$

is obtained for the orthotropic film. In the case of an effective transversal isotropy substituting Eqs. (16) to (15) into (14), (15) and finally into (12) yields

$$U_{AC} = -\frac{hgC^* \left( 1 - v^S \right)}{E^S} \left\{ \sigma_{11} + \sigma_{22} \right\} \tag{17}$$

## 6   Asymptotic crack tip near field

In the Linear Elastic Fracture Mechanics (LEFM) the asymptotic fields ($r{\rightarrow}0$) of displacements, stresses and strains near the crack tip are expressed in terms of stress intensity factors (K-factors) ([Gross and Seelig (2007)], [Kuna (2008)]). At finite distance to the crack tip higher order terms are taken into account, e.g. a non-singular constant stress named T-stress acting parallel to the crack. The stress tensor components are

$$
\begin{aligned}
\sigma_{11} = & \frac{K_I}{\sqrt{2\pi r}}\cos\left(\frac{\varphi}{2}\right)\left(1-\sin\left(\frac{\varphi}{2}\right)\sin\left(\frac{3\varphi}{2}\right)\right)- \\
& \frac{K_{II}}{\sqrt{2\pi r}}\sin\left(\frac{\varphi}{2}\right)\left(2+\cos\left(\frac{\varphi}{2}\right)\cos\left(\frac{3\varphi}{2}\right)\right)+T
\end{aligned}
\tag{18}
$$

$$
\begin{aligned}
\sigma_{22} = & \frac{K_I}{\sqrt{2\pi r}}\cos\left(\frac{\varphi}{2}\right)\left(1+\sin\left(\frac{\varphi}{2}\right)\sin\left(\frac{3\varphi}{2}\right)\right)+ \\
& \frac{K_{II}}{\sqrt{2\pi r}}\sin\left(\frac{\varphi}{2}\right)\cos\left(\frac{\varphi}{2}\right)\cos\left(\frac{3\varphi}{2}\right)
\end{aligned}
\tag{19}
$$

$$
\begin{aligned}
\sigma_{12} = & \frac{K_I}{\sqrt{2\pi r}}\sin\left(\frac{\varphi}{2}\right)\cos\left(\frac{\varphi}{2}\right)\cos\left(\frac{3\varphi}{2}\right)+ \\
& \frac{K_{II}}{\sqrt{2\pi r}}\cos\left(\frac{\varphi}{2}\right)\left(1-\sin\left(\frac{\varphi}{2}\right)\sin\left(\frac{3\varphi}{2}\right)\right)
\end{aligned}
\tag{20}
$$

with $-\pi \leq \varphi \leq \pi$.

The $K_I$ and $K_{II}$ represent the two in-plane crack opening modes I and II. The polar coordinate system $(r, \varphi)$ has its origin at the crack tip and on the ligament $\varphi = 0$. In order to obtain the relationship between the fracture mechanical quantities $K_I$, $K_{II}$, $T$ and the voltage at the piezoelectric film, the Eqs. (21) to (20) are substituted into Eqs. (19) and (17), respectively. According to Williams ([Williams (1957)], [Kuna (2008)]), the stresses in a cracked body are represented by an infinite series where higher order terms ($n > 2$) account for larger distances from the crack tip compared to the asymptotic solution (21) to (20). This extension may be crucial for remote electrodes. Using this general representation of the stress state, one obtains for the orthotropic case:

$$
\begin{aligned}
U_{AB} = C_0 \sum_{n=1}^{\infty} r^{\frac{n}{2}-1}\big(a_n\left(M_{11}^{(n)}f_I+M_{22}^{(n)}f_{II}+M_{12}^{(n)}f_{III}\right)+ \\
b_n\left(N_{11}^{(n)}f_I+N_{22}^{(n)}f_{II}+N_{12}^{(n)}f_{III}\right)\big),
\end{aligned}
\tag{21}
$$

with

$$C_0 = -\frac{hg}{E^S},$$

$$f_I = \cos^2 \beta \left(C_1 - v^S C_2\right) + \sin^2 \beta \left(C_2 - v^S C_1\right),$$

$$f_{II} = \sin^2 \beta \left(C_1 - v^S C_2\right) + \cos^2 \beta \left(C_2 - v^S C_1\right),$$

$$f_{III} = \left(1 + v^S\right) \left(C_1 - C_2\right) \sin(2\beta),$$

$$M_{11}^{(n)} = \frac{n}{2} \left\{ \left[2 + (-1)^n + \frac{n}{2}\right] \cos\left[\left(\frac{n}{2} - 1\right) \varphi\right] - \left(\frac{n}{2} - 1\right) \cos\left[\left(\frac{n}{2} - 3\right) \varphi\right] \right\},$$

$$N_{11}^{(n)} = \frac{n}{2} \left\{ \left[-2 + (-1)^n - \frac{n}{2}\right] \sin\left[\left(\frac{n}{2} - 1\right) \varphi\right] + \left(\frac{n}{2} - 1\right) \sin\left[\left(\frac{n}{2} - 3\right) \varphi\right] \right\},$$

$$M_{22}^{(n)} = \frac{n}{2} \left\{ \left[2 - (-1)^n - \frac{n}{2}\right] \cos\left[\left(\frac{n}{2} - 1\right) \varphi\right] + \left(\frac{n}{2} - 1\right) \cos\left[\left(\frac{n}{2} - 3\right) \varphi\right] \right\},$$

$$N_{22}^{(n)} = \frac{n}{2} \left\{ \left[-2 - (-1)^n + \frac{n}{2}\right] \sin\left[\left(\frac{n}{2} - 1\right) \varphi\right] - \left(\frac{n}{2} - 1\right) \sin\left[\left(\frac{n}{2} - 3\right) \varphi\right] \right\},$$

$$M_{12}^{(n)} = \frac{n}{2} \left\{ \left(\frac{n}{2} - 1\right) \sin\left[\left(\frac{n}{2} - 3\right) \varphi\right] - \left[\frac{n}{2} + (-1)^n\right] \sin\left[\left(\frac{n}{2} - 1\right) \varphi\right] \right\},$$

$$N_{12}^{(n)} = \frac{n}{2} \left\{ \left(\frac{n}{2} - 1\right) \cos\left[\left(\frac{n}{2} - 3\right) \varphi\right] - \left[\frac{n}{2} - (-1)^n\right] \cos\left[\left(\frac{n}{2} - 1\right) \varphi\right] \right\}.$$

The $a_n, b_n$ are coefficients of the $n$-th eigenfunction of the crack field solution. Their values for $n = 1, 2$ correspond to

$$a_1 = \frac{K_I}{\sqrt{2\pi}}, \quad b_1 = -\frac{K_{II}}{\sqrt{2\pi}} \text{ and } a_2 = \frac{T}{4}.$$

Within this general framework of describing the stress state, Eqs. (21) to (20) represent the special case $n = [1, 2]$. The case of transverse isotropy of the PVDF film looks much simpler:

$$U_{AC} = C_0^* \left\{ \sum_{n=1}^{\infty} n r^{\frac{n}{2} - 1} \left[a_n \cos \alpha_n - b_n \sin \alpha_n\right] \right\}, \tag{22}$$

with

$$C_0^* = -\frac{2hgC^* \left(1 - v^S\right)}{E^S}, \quad \alpha_n = \left(\frac{n}{2} - 1\right) \varphi.$$

With the equations (21) and (22), respectively the electrical potential difference at a point-shaped electrode located at the position $(r, \varphi)$ in the polar coordinate system related to the crack tip can be calculated if the load situation is known.

## 7  Solution of the inverse problem

Due to strains at the specimen surface, potential differences are induced at any position of the piezoelectric film, which can be measured in principle. If the loading situation at the crack tip is to be determined based on these measured potentials the solution of an inverse boundary value problem of the theory of elasticity is required. If the crack position with respect to the film is known, K-factors, $T$-stress and optionally further terms of the crack solution are the unknown quantities to be determined. If the problem is limited $a_n, b_n$ to $K_I$, $K_{II}$ and $T$-stress, there are three unknowns requiring a system of at least three equations associated with three measuring points. In this case a linear system of equations with unique solution is obtained.

However, the practical application of this sensor concept is focussed on the detection of unknown crack paths. This means that the crack position with respect to the film is not known and the coordinates of the measuring points $(r_i, \varphi_i)$ in the crack coordinate system $(x, y)$ thus are not available. Introducing a local coordinate system $(x', y')$ related to the film (Fig. 5), the position of any measuring point can be calculated by coordinate transformation to the crack coordinate system $(x, y)$. As the coordinates of the electrodes with respect to the film are known, the fracture quantities are complemented by three more unknowns $(x_0, y_0, \beta)$ describing the film position with respect to the crack faces (Fig. 5). Thus, three more measuring points and equations need to be considered.

The following equations relate the two coordinate systems:

$$x_i = x_i' \cos\beta - y_i' \sin\beta + x_0, \tag{23}$$

$$y_i = x_i' \sin\beta + y_i' \cos\beta + y_0, \tag{24}$$

$$r_i = \sqrt{x_i^2 + y_i^2}, \tag{25}$$

$$\begin{aligned} \varphi_i &= \arccos\frac{x_i}{r_i} 0 \leq \varphi_i \leq \pi \\ \varphi_i &= -\arccos\frac{x_i}{r_i} - \pi \leq \varphi_i < 0 \end{aligned}. \tag{26}$$

In connection with equations (21) and (22), a nonlinear algebraic equation including six unknowns is obtained. For the sake of a unique solution at least six independent equations are required, which in connection with at least six electrodes enable the calculation of SIFs, $T$-stress and the coordinates of the crack tip. The measuring points have to be sufficiently close to the crack tip in order not to leave the range of validity of equations (21) to (20) or (21) and (22) for finite $n$. Since a manifold of solutions exists due to the nonlinearity of the system of equations,

some more measuring points need to be involved into the evaluation. In principle, the nonlinear algebraic system is solvable applying standard algorithms such as Newton's method, however the initial approximations must be very close to the final values, in order not to be captured in local minima. Therefore, a solution is sought in terms of a nonlinear optimization problem. To solve the nonlinear system of equations two different procedures are applied: the principal axis method [Brent (1973)] and the Levenberg-Marquardt method [Moré (1977)]. The principal axis method has been developed by R.P. Brent and is known as one of the best optimization algorithms not needing any information on the gradient of the function. The method possesses a few special features compared to other algorithms, like e.g. the assumption that local minima evolve from second order functions. The principal axis method exhibits some advantages with respect to the Levenberg-Marquardt procedure. It proves to be e.g. less sensitive towards the initial values of the iteration and goes along with a higher numerical robustness. The testing of both methods is based on numerical simulations of the structure – sensor – system and therewith calculated electrical potentials. The results are compared with each other in the next section.

Besides these two nonlinear optimization algorithms, the feasibility of applying neural networks to the solution of the problem under consideration is investigated. This technique is frequently used in order to solve highly nonlinear inverse problems [Nguyen (1993); Xia and Feng (2007)]. An artificial neural network commonly consists of several layers, where the first layer represents the input information and the last one supplies the output data. The weights of the connections between different neurons are calculated based on a training algorithm, e.g. the backpropagation-algorithm, in which all training data sets are propagated repeatedly in arbitrary order. For the calculations outlined in the following section, the software package SNNS (Stuttgart Neuronal Network Simulator [Zell et.al. (1995)]) was used, which is freely accessible and feasible for the development of a variety of net variants.

## 8 Testing of the solution algorithms

The numerical solution of the boundary value problem of the cracked structure with applied sensor film is achieved with the commercial Finite Element (FE) code ABAQUS. It is used to test the analysis methods as well as to verify the efficiency of the overall concept. In Fig. 6 a scheme of the model of a plate with a straight edge crack is presented.

The small dark areas on the surface represent sensor arrays which are applied to the slightly gray PVDF film. In the FE model the latter is modelled as an orthotropic piezoelectric material. At the film-structure interface the electric potential is set
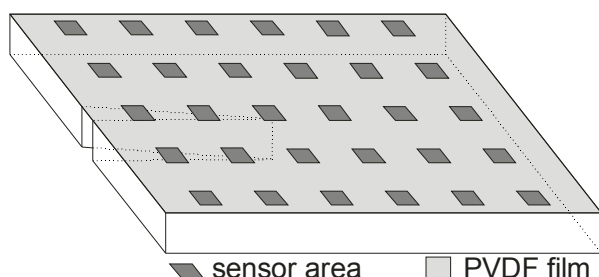
Figure 6: Schematic of the system structure-film-electrodes

to zero. Relative motion between the film and the plate is neglected, i.e. there is a fixed constraint with $g = 1$. Due to the high ductility and failure strain of the PVDF, it is assumed that the film is not ruptured by the crack opening locally bearing large deformations. Calculations have proven that the influence on the potentials at sensors lying close to the crack path can be neglected.

The sensor concept is verified at a plate specimen (Fig. 7) holding the dimensions (width×height×length) $10 \times 250 \times 750$ mm featuring an edge crack of length 25 mm, which is loaded in different ways.

The film has the dimensions (w×h×l) $0.1 \times 50 \times 50$ mm exhibiting 49 sensors with an area $0.5 \times 0.5$ mm each, being arranged at regular distances of 5 mm to each other. The condition of homogeneous potentials at the area of each electrode implicitly effectuates an integration of local potentials there in the FE-model.

For the plate material, the elastic constants of steel $E^S = 210$ GPa and $v^S = 0.3$ have been chosen. First, the results from the nonlinear optimization algorithms are discussed. In the following, some abbreviations are introduced: RS – reference solution, PA – principal axis method, LM – Levenberg-Marquardt method, IV – initial values. The calculations with ABAQUS have been carried out under different loading conditions, i.e. pure mode I and II as well as mixed mode. In addition, the position of the film with respect to the crack including the angle to each other were varied. The electric potentials emanating from the simulations were considered to be measured potentials and served as input values for the testing of the mathematical sensor concept. Those sensors being directly located above the crack faces were not used for the evaluation. In the Tables 1 to 5 some results of the calculations are presented. Applying the PA, three rather than the two terms of the crack tip near field solution depicted in the Eqs. (21) to (20) have been taken into account. On the other hand, applying the LM only two terms of the series were used with the exception of Table 3.

It can be concluded from the results that in the case of a predominant mode I loading (Tables 1, 2, 4 and 5) being characteristic for fatigue crack growth, the solution found from the inverse problem is in good agreement with the reference solution. Especially the coordinates $(x_0, y_0, \beta)$ being relevant for the crack position are very well determined. Although the calculated $T$-stress mostly has significant deviations from the reference solution, the errors in the more important $K_I-$ factor are never above 10%. Generally it was found that the PA in comparison to the LM is less sensitive towards the starting value of the iteration. It was also observed for pure mode I loading with a straight crack path $(\beta = 0)$ that the values from the sensors being located directly in front of the crack are completely sufficient to get close to the correct solution. In the case of a predominant mode II (Table 3) a satisfactory agreement could not be obtained. Here, the choice of the initial values and the number of terms used for the crack tip near field solution play an important role. The reason could be the deviation of the analytically predicted stresses $\sigma_{11}$ from those actually calculated for the specimen using the FEM. A difference of e.g. 5 MPa according to Eq. (21) causes a deviation of one volt.

Finally, some results based on calculations with a neural network are presented. The data basis for the training procedure of the network is presented in Table 6. Two sets of data have been chosen including the six relevant parameters of crack position and loading and the respective electric potentials. The first layer comprises 16 input neurons. Attempts to include smaller numbers of neurons have not been successful. The second and third layer consists of 10 neurons each and the output neurons correspond to the six unknowns.
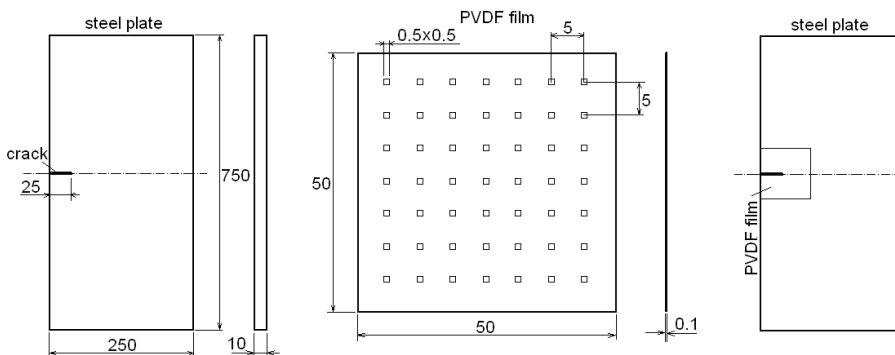


Figure 7: Plate with crack and sensor array with electrodes (dimensions in mm)

In Table 7 results are presented for four different parameter sets comparing the respective reference solution (RS) to the solution emerging from the neural network

Table 1: Solution for two different initial values IV (pure mode I loading)

| method unknown | RL | IV | PA | LM | IV | PA | LM |
|---|---|---|---|---|---|---|---|
| $x_0$ [mm] | -25,00 | -22,00 | -24,60 | -25,26 | -28,00 | -25,24 | -25,13 |
| $y_0$ [mm] | -25,00 | -22,00 | -25,00 | -25,01 | -28,00 | -25,00 | -24,97 |
| $\beta$ [deg] | 0,00 | 3,00 | 0,00 | 0,01 | -5,00 | 0,00 | 0,01 |
| $K_I$ [MPa$\sqrt{\text{mm}}$] | 508,00 | 550,00 | 464,43 | 446,66 | 600,00 | 446,84 | 441,98 |
| $K_{II}$ [MPa$\sqrt{\text{mm}}$] | 0,00 | 50,00 | 0,00 | 0,05 | 100,00 | 0,00 | -1,18 |
| $T$ [MPa] | -20,00 | -10,00 | -12,17 | -15,37 | -30,00 | -12,55 | -15,23 |

Table 2: Solution for two different initial values IV (mixed mode loading)

| method unknown | RL | IV | PA | LM | IV | PA | LM |
|---|---|---|---|---|---|---|---|
| $x_0$ [mm] | -25,00 | -22,00 | -24,41 | -24,46 | -28,00 | -24,41 | -25,27 |
| $y_0$ [mm] | -25,00 | -22,00 | -25,05 | -24,69 | -28,00 | -25,05 | -24,58 |
| $\beta$ [deg] | 0,00 | 3,00 | 0,34 | -0,28 | -5,00 | 0,34 | -1,12 |
| $K_I$ [MPa$\sqrt{\text{mm}}$] | 1194,00 | 1000,00 | 1142,22 | 1119,64 | 900,00 | 1142,22 | 1035,64 |
| $K_{II}$ [MPa$\sqrt{\text{mm}}$] | 123,00 | 150,00 | 43,04 | 25,16 | 90,00 | 43,04 | 35,40 |
| $T$ [MPa] | -59,00 | -65,00 | -28,96 | -39,03 | -40,00 | -28,96 | -34,05 |

Table 3: Solution for two different initial values IV (pure mode II loading)

| method / unknown | RL | IV | PA | LM | IV | PA | LM |
|---|---|---|---|---|---|---|---|
| $x_0$ [mm] | -25,00 | -23,00 | -25,75 | -24,44 | -25,00 | -25,52 | -24,51 |
| $y_0$ [mm] | -25,00 | -23,00 | -24,38 | -24,50 | -25,00 | -24,27 | -25,50 |
| $\beta$ [deg] | 0,00 | 5,00 | -2,42 | 2,66 | 0,00 | -2,05 | 1,48 |
| $K_I$ [MPa$\sqrt{\text{mm}}$] | -202,00 | -100,00 | -175,74 | -93,82 | 0,00 | -173,38 | -129,41 |
| $K_{II}$ [MPa$\sqrt{\text{mm}}$] | 85,00 | 100,00 | 43,64 | 64,18 | 85,00 | 51,48 | 47,09 |
| $T$ [MPa] | 10,00 | 15,00 | 4,14 | 2,51 | 10,00 | 4,06 | 4,09 |

Table 4: Solution for two different initial values IV (mixed mode loading)

| method / unknown | RL | IV | PA | LM | IV | PA | LM |
|---|---|---|---|---|---|---|---|
| $x_0$ [mm] | -28,96 | -29,00 | -28,41 | -27,83 | -31,00 | -28,44 | -26,43 |
| $y_0$ [mm] | -20,28 | -21,00 | -20,90 | -20,96 | -23,00 | -21,50 | -23,64 |
| $\beta$ [deg] | -10,00 | -11,00 | -10,58 | -10,44 | -12,00 | -9,16 | -4,12 |
| $K_I$ [MPa$\sqrt{\text{mm}}$] | 501,00 | 510,00 | 491,19 | 444,78 | 550,00 | 500,06 | 416,02 |
| $K_{II}$ [MPa$\sqrt{\text{mm}}$] | 60,00 | 60,00 | 68,75 | 62,80 | 80,00 | 66,11 | 79,21 |
| $T$ [MPa] | -17,00 | -20,00 | -7,41 | -8,54 | -25,00 | -5,67 | -3,43 |

Table 5: Solution for two different initial values IV (pure mode I loading), crack position different from the one in Table 1

| method unknown | RL | IV | PA | LM | IV | PA | LM |
|---|---|---|---|---|---|---|---|
| $x_0$ [mm] | -20,00 | -17,00 | -19,53 | -19,26 | -22,00 | -19,53 | -19,40 |
| $y_0$ [mm] | -25,00 | -22,00 | -25,00 | -24,98 | -27,00 | -25,00 | -24,99 |
| $\beta$ [deg] | 0,00 | 3,00 | 0,00 | -0,44 | -3,00 | 0,00 | 0,02 |
| $K_I$ [MPa$\sqrt{\text{mm}}$] | 508,00 | 400,00 | 484,50 | 482,96 | 600,00 | 484,50 | 481,73 |
| $K_{II}$ [MPa$\sqrt{\text{mm}}$] | 0,00 | 10,00 | 0,00 | -0,02 | -10,00 | 0,00 | -0,20 |
| $T$ [MPa] | -20,00 | -25,00 | -15,44 | -18,14 | -15,00 | -15,44 | -18,01 |

Table 6: Data sets for the training procedure of the neural network

|  | set 1 | set 2 |
|---|---|---|
| $x_0$ [mm] | -27 | -23 |
| $y_0$ [mm] | -27 | -23 |
| $\beta$ [deg] | -3 | 3 |
| $K_I$ [MPa$\sqrt{\text{mm}}$] | 400 | 600 |
| $K_{II}$ [MPa$\sqrt{\text{mm}}$] | -100 | 100 |
| $T$ [MPa] | -20 | 20 |

Table 7: Solution of the inverse problem using a neural network

| | RS | NN | RS | NN | RS | NN | RS | NN |
|---|---|---|---|---|---|---|---|---|
| $x_0$ [mm] | -23,00 | -23,00 | -27,00 | -26,98 | -25,00 | -25,56 | -23,00 | -26,59 |
| $y_0$ [mm] | -23,00 | -23,01 | -27,00 | -27,00 | -25,00 | -25,80 | -23,00 | -27,00 |
| $\beta$ [deg] | -3,00 | -3,00 | 3,00 | 2,99,00 | 0,00 | -1,50 | 3,00 | 1,01 |
| $K_I$ [MPa$\sqrt{\text{mm}}$] | 400,00 | 400,00 | 600,00 | 600,00 | 500,00 | 480,00 | 100,00 | 400,05 |
| $K_{II}$ [MPa$\sqrt{\text{mm}}$] | -100,00 | -100,00 | 100,00 | 100,00 | 0,00 | -20,00 | 0,00 | 0,08 |
| $T$ [MPa] | -20,00 | -19,99 | 20,00 | 20,00 | 0,00 | -10,00 | -20,00 | -19,99 |

(NN). The relation between the parameters and the electric potential is based on the analytical considerations outlined in sections 5 and 6 in order to decouple the testing of the NN method from possible numerical inaccuracy. The first two data sets corresponding to the sets used for the training of the neuronal network (Table 6) entail perfect results as expected. For the third example, input data have been chosen lying between the boundaries of the training sets. In this case, results for the crack tip coordinates $(x_0, y_0)$ and the $K_I$-factor, being the technically most interesting parameters, are still very good. For the angle $\beta$, $K_{II}$ and the $T$-stress, the coincidence with the reference solution is worse, however the total values of these quantities are small. The fourth example investigates the case that one crack parameter, e.g. $K_I$ is chosen outside the interval prescribed by the training sets. Whereas $x_0, y_0$, $K_{II}$ and $T$ come out very well, the inclination angle $\beta$ is rather imprecise. Yet more important is the deviation of $K_I$ from the reference value which is four times smaller. It is the outstanding disadvantage of the method that the range of parameters is restricted by the training sets. To account for a wider range of values, more neurons have to be incorporated into the network. The total error, however, is only gradually reduced.

## 9    Summary

The strains on the surface of a cracked specimen, resulting from a mechanical loading, cause deformations at the firmly adhered piezoelectric PVDF film. Thus, on its surface, charges and electric potentials, respectively, are generated which are measured at discrete locations using an array of electrodes. The aim of the presented sensor concept is to identify the crack position and the fracture mechanical quantities from these potential values. Concerning mechanical properties, the polymeric PVDF material has significant advantages compared to piezoelectric ceramics. The sensor concept is particularly suitable for monitoring cracks in plate and shell structures under conditions of linear elastic fracture mechanics. Here, especially fatigue crack growth plays an important role, where the crack paths usually exhibit large radii of curvature and the mode I crack opening

mechanism dominates. In this case, the solution of the inverse problem provides very good results. An accuracy better than 10% is achieved concerning the crack position and the value of $K_I$. The best experience was gained with the principal axis method. Pure mode II loading, however, still does not lead to good predictions of K-factors and crack positions.

## References

**Brent R.P.** (1973): *Algorithms for Minimization without Derivatives*, Prentice-Hall, Englewood Cliffs, New Jersey.

**Danz R.; Geiss D.** (1987): Struktur und Eigenschaften piezo- und pyroelektrischer Polymerfolien. *Acta Polymeria*, 38, No. 6, pp. 399-406.

**Dally J.W.; Sanford R.J.** (1988): Strain gage methods for measuring the opening mode stress-intensity factor KI. *Experimental Mechanics*, 27, pp. 381-388.

**Dally J.W.; Sanford R.J.** (1990): Measuring the stress intensity factor for propagating cracks with strain gages. *Journal of Testing and Evaluation*, 18, pp. 240-249.

**Fujimoto Y.; Shintaku E.; Pirker G.; Liu G.** (2003): Piezoelectric sensor for stress intensity factor measurement of two dimensional cracks. *Engineering fracture Mechanics*, 70, pp. 1203-1218.

**Fujimoto Y.; Shintaku E.; Pirker G.; Tanaka Y.** (2003): Stress Intensity Factor Measurement of Two-Dimensional Cracks by the Use of Piezoelectric Sensor. *JSME International Journal, Series A*, 46, pp. 567-574.

**Fujimoto Y.; Liu G.; Tanaka Y.; In E.** (2004): Stress Intensity Factor Measurement of Cracks Using a Piezoelectric Element. *Experimental Mechanics*, 44, pp. 320-325.

**Gama A.L.; Morikawa S.R.K.** (2008): Monitoring fatigue crack growth in compact tension specimens using piezoelectric sensors. *Experimental Mechanics*, 48, pp. 247-252.

**Gross D.; Seelig T.** (2007): *Bruchmechanik (mit einer Einführung in die Mikromechanik)*, Springer, Berlin, 4th edition.

**Honda T.; Sasaki T.; Yoshihisa E.** (2002): A study to improve the measurement accuracy of stress intensity factor by the infrared method. In: Damage and Fracture Mechanics VII, C. A. Brebbia, S. I. Nishida (eds.), WIT Press.

**Irwin G.R.** (1957): Analysis of stresses and strain near the end of a crack traversing a plate. *Journal of Applied Mechanics*, 24, pp. 361-388.

**Kamleitner A.; Faber T.; Starossek U.** (2005): Einsatz bruchmechanischer Methoden zur Bestimmung der Restnutzungsdauer von Windenergieanlagen. *Stahlbau*, 74, pp. 399-405.

**Kuna M.** (2008): *Numerische Beanspuchungsanalyse von Rissen*, Vieweg+Teubner, Wiesbaden, 1st edition.

**Kurosaki S.; Suzuki T.; Kusuda M.** (2002): The fatigue crack propagation monitoring by using piezo electric polymer film. *Research Reports of Tokyo National College of Technilogy*, 33, pp. 45-48.

**Kwun H.; Light G.M.; Kim S.-Y., Spinks R.L.** (2002): Magnetostrictive sensor for active health monitoring in structures. In: Proc. of SPIE-The Internation Society for Optical Engineering, 4702, pp. 282-288.

**Lange G.** (1983): Systematische Beurteilung technischer Schadensfälle, DGM, Oberursel, 2nd edition.

**Lu H.; Chiang F.P.** (1993): Photoelastic determination of stress intensity factor of an interfacial crack in a bi-material. *Journal of Applied Mechanics*, 60, pp. 93-100.

**McNeill S.R.; Peters W.H.; Sutton M.A.** (1987): Estimation of stress intensity factor by digital image correlation. *Engineering Fracture Mechanics*, 28, pp. 101-112.

**Moré J.J.** (1977): The Levenberg-Marquardt Algorithm: Implementation and Theory, *Numerical Analysis*, ed. G. A. Watson, Lecture Notes in Mathematics, 630, Springer, pp. 105-116.

**Nguyen T.T.** (1993): Neuronal network architecture for solving nonlinear equation systems. *Electronics Letters*, 29, pp. 1403-1405.

**Putra I.S.** (2000): Some experiences in using the K-gage to measure stress intensity factors. In: Damage and Fracture Mechanics VI, A. P.S. Selvadurai, C.A. Brebbia (eds.), WIT Press, pp. 83-92.

**Rethore J.; Gravouil A.; Morestin F.; Combescure A.** (2005): Estimation of mixed-mode stress intensity factors using digital image correlation and an interaction integral. *International Journal of Fracture*, 132, pp. 65-79.

**Roh Y.; Varadan V.V.; Varadan V.K.** (2002): Characterization of All the Elastic, Dielectric, and Piezoelectric Constants of Uniaxialy Oriented Poled PVDF Films. *IEEE Transaction On Ultrasonics, Ferroelectrics, And Frequency Control*, 49, No. 6, pp. 836-847.

**Roux S.; Hild F.** (2006): Stress intensity factor measurements from digital image correlation: postprocessing and integrated approaches. *International Journal of Fracture*, 140, pp. 141-157.

**Saka M.; Nakayama M.; Kaneko T.; Abe H.** (1991): Measurement of stress-intensity factor by means of A-C potential drop technique. *Experimental Mechanics*, 31, pp. 209-212.

**Shiratori M.; Miyoshi T.; Nakanishi T.,; Noda T.; Harada M.** (1990): Detection of cracks and measurement of stress intensity factors by infrared video system. *JSME Internation Journal. Series A, Solid mechanics and material engineering*, 33, pp. 400-408.

**Shozu M.; Ikeda R.; Hirose Y.** (2002): Measurement of stress intensity factor under Mode I, II and III loadings by caustics method. In: Proc. Symposium on X-Ray Studies on Mechanical Behavior of Materials, 38, pp. 123-127.

**Singh R.P.; Shuka A.** (1996): Characterisation of isochromatic fringe patterns for a dynamically propagating interface crack. *International Journal of Fracture*, 76, pp. 293-310.

**Williams, M.L.** (1957): On the stress distribution at the base of a stationary crack. *Journal of Applied Mechanics*, 24, pp. 109-114.

**Xia Y.; Feng G.** (2007): A new neuronal network for solving nonlinear projection equations. *Neuronal Networks*, 20, pp. 577-589.

**Zell A. *et.al.*** (1995): SNNS Stuttgart Neuronal Network Simulator, User Manual, Version 4.1, Institute for parallel and distributed high performance systems.

## Appendix

*Material constants of PVDF in Voigt-notation*

$$[c] = \begin{pmatrix} 3610 & 1610 & 1420 & 0 & 0 & 0 \\ 1610 & 3130 & 1310 & 0 & 0 & 0 \\ 1420 & 1310 & 1599.1 & 0 & 0 & 0 \\ 0 & 0 & 0 & 550 & 0 & 0 \\ 0 & 0 & 0 & 0 & 579.1 & 0 \\ 0 & 0 & 0 & 0 & 0 & 690 \end{pmatrix} \left[ \frac{N}{mm^2} \right],$$

$$[e] = \begin{pmatrix} 0 & 0 & 0 & 0 & -12.102 & 0 \\ 0 & 0 & 0 & -12.222 & 0 & 0 \\ 11.286 & -11.988 & -28.421 & 0 & 0 & 0 \end{pmatrix} \left[ \frac{nC}{mm^2} \right],$$

$$[\kappa] = \begin{pmatrix} 6.5 & 0 & 0 \\ 0 & 8.2 & 0 \\ 0 & 0 & 7.1275 \end{pmatrix} \cdot 10^{-5} \left[ \frac{nC}{Vmm} \right].$$

*Representation of material tensors in Voigt-notation*

$$\{\sigma\} = \begin{Bmatrix} \sigma_{11} \\ \sigma_{22} \\ \sigma_{33} \\ \sigma_{23} \\ \sigma_{31} \\ \sigma_{12} \end{Bmatrix}, \quad \{\varepsilon\} = \begin{Bmatrix} \varepsilon_{11} \\ \varepsilon_{22} \\ \varepsilon_{33} \\ 2\,\varepsilon_{23} \\ 2\,\varepsilon_{31} \\ 2\,\varepsilon_{12} \end{Bmatrix}, \quad \{D\} = \begin{Bmatrix} D_1 \\ D_2 \\ D_3 \end{Bmatrix},$$

$$\{E\} = \begin{Bmatrix} E_1 \\ E_2 \\ E_3 \end{Bmatrix}, \quad [\kappa] = \begin{bmatrix} \kappa_{11} & 0 & 0 \\ 0 & \kappa_{22} & 0 \\ 0 & 0 & \kappa_{33} \end{bmatrix},$$

$$[e] = \begin{bmatrix} 0 & 0 & 0 & 0 & e_{15} & 0 \\ 0 & 0 & 0 & e_{24} & 0 & 0 \\ e_{31} & e_{32} & e_{33} & 0 & 0 & 0 \end{bmatrix},$$

$$[c] = \begin{bmatrix} c_{11} & c_{12} & c_{13} & 0 & 0 & 0 \\ c_{12} & c_{22} & c_{23} & 0 & 0 & 0 \\ c_{13} & c_{23} & c_{33} & 0 & 0 & 0 \\ 0 & 0 & 0 & c_{44} & 0 & 0 \\ 0 & 0 & 0 & 0 & c_{55} & 0 \\ 0 & 0 & 0 & 0 & 0 & c_{66} \end{bmatrix}.$$